On the influence of ϰ-carbides on the low-cycle fatigue behavior of high-Mn light-weight steels

T. Wegener[1*], C. Haase[2], A. Liehr[1], T. Niendorf[1]

1 Institut für Werkstofftechnik, Metallische Werkstoffe, Universität Kassel,
Mönchebergstraße 3, 34125 Kassel, Germany
2 Chair Materials Engineering of Metals, Steel Institute, RWTH Aachen University,
Intzestraße 1, 52072 Aachen, Germany

Abstract

High-manganese light-weight steels offer a great potential for structural purposes in the mobility sector due to their reduced density combined with outstanding mechanical properties. As many of the envisaged applications of these materials will suffer from cyclic loading during their service life, the fundamentals of their fatigue behavior must be studied extensively. In the present work, the low-cycle fatigue (LCF) properties of an austenitic Fe-29.8Mn-7.65Al-1.11C light-weight steel were investigated. Two microstructurally different conditions are directly compared: a homogenized, fully austenitic condition and an aged, austenitic, ϰ-carbide-containing condition. Results obtained by total strain-controlled fatigue tests are discussed based on microstructural insights revealed by scanning electron microscopy and synchrotron diffraction analysis. Although fatigue properties are improved upon aging due to ϰ-carbide formation for lower strain amplitudes as compared to homogenized counterparts, the cyclic deformation behavior is characterized by cyclic softening at increased strain levels. Shearing of the ϰ-carbides and their mechanical dissolution due to the onset of plastic deformation are found to be the underlying mechanism. Determination of LCF parameters for both conditions was realized by evaluation of the fatigue life by the Coffin-Manson law and Basquin equation, eventually providing explanations for the Masing and non-Masing behavior of the aged and homogenized condition, respectively, as determined by analysis of half-life hysteresis loops.

Keywords: Fe-MnAl-C, Light-weight steel, Low-Cycle Fatigue, ϰ-carbides, Microstructure

1. Introduction

In line with the ongoing developments in the field of light-weight design, a remarkable demand for advanced light-weight steels being characterized by superior mechanical properties, i.e. a high strength combined with an excellent ductility, prevails in many industrial fields such as the mobility sector. Enabled by the high level of specific strength, these steels allow for the design of crash-relevant body structures leading to a weight reduction and, thus, to an improved fuel efficiency as well as a reduced CO_2 emission.

In recent years austenitic high-manganese steels (HMnS) have been intensively studied as a representative of advanced light-weight steels because of their outstanding properties overcoming the strength-ductility tradeoff [1]. In the group of HMnS mainly two types of steels have attracted high scientific and commercial interest, i.e., Twinning-Induced Plasticity (TWIP) as well as Transformation-Induced Plasticity (TRIP) steels. Based on their alloying concept and the resulting stacking fault energies (SFE), a high strain hardening rate up to relatively high strain levels is achieved by activation of multiple deformation mechanisms: in addition to planar dislocation glide, mechanically driven solid to solid phase transformation from austenite to either α'-martensite or ε–martensite prevails in low-SFE (< 20 mJ/m^2) TRIP steels, whereas deformation-induced twinning is the dominant mechanism at higher SFE values (~ 20-40 mJ/m^2) in TWIP steels [2–5].

By adding high amounts of Al, another subgroup of the HMnS, referred to as high-Mn light-weight steels or light-weight Fe-Mn-Al-C alloys, has become one of the most promising candidates in this field. As a reduction in density by 1.5% per 1 wt% addition of Al is obtained, these steels are characterized by a low density, rendering them as light-weight material [6–8]. Being already developed in the 1950s as a substitute for stainless Fe-Cr-Ni steels [7], light-weight Fe-Mn-Al-C alloys, commonly characterized by high manganese (18-30 wt%) and aluminum contents (< 12 wt%) with the addition of silicon (< 3 wt%) along with carbon (up to 2 wt%), were recently revisited [1,6,9,10]. Besides their reduced specific weight, high-Mn light-weight steels are well-known for outstanding mechanical properties exhibiting a superior strength-ductility balance, i.e. a yield strength (YS), ultimate tensile strength (UTS) as well as elongation to failure of up to 1 GPa, 1.5 GPa and 100 %, respectively [6–8,11–15]. As a result of these properties Fe-Mn-Al-C alloys are used in numerous applications, i.e., cryogenic and corrosive environments as well as at high temperatures suffering oxidation. Furthermore, they offer a great potential for structural purposes, particularly in the automotive industry [7]. For conventional high-Mn TWIP steels improvement of mechanical properties as a result of grain refinement was achieved by combined thermomechanical rolling routes or special severe plastic

deformation (SPD) techniques such as Equal Channel Angular Pressing (ECAP) [16–19]. However, these special techniques still offer a great potential in the field of high-Mn light-weight steels, as they have not been in focus yet.

Due to the different fractions of alloying elements, where Al acts as ferrite stabilizer and manganese and carbon are known to stabilize the austenic phase, metallurgical and microstructural properties of high-Mn light-weight steels are very complex. Depending on chemical composition and heat-treatment, the various compositions can be classified into different categories, i.e. single-phase austenitic (γ) or ferritic (δ) steels, dual-phase steels (e.g. consisting of combinations of γ, δ and ternary $\varkappa$-carbides of type $(Fe,Mn)_3AlC_x$ with ordered $E2_1$ perovskite structure [20–22]) and triplex steels ($\gamma + \delta + \varkappa$-carbides) [7,8,23].

As a result of the relatively high Al content, high-Mn light-weight steels are, compared to their TWIP or TRIP steel counterparts, characterized by medium to high SFE in a range between $80 \, \mathrm{mJ/m^2}$ and $120 \, \mathrm{mJ/m^2}$ [7,24,25]. Thus, suppression of both, TWIP- as well as TRIP-effect has been observed, leading to dislocation glide being the dominant deformation mechanism governing plastic deformation instead [10,24,26]. Usually, dislocations are known to easily change their glide planes via cross-slip resulting in deformation by wavy glide in high SFE fcc materials [27–29]. However, despite of chemical composition and heat treatment, deformation in light-weight Fe-Mn-Al-C alloys is restricted to planar dislocation glide [7–9,21,22,30]. Accordingly, most studies reporting on high-Mn light-weight steels focused on explanation of the unique interplay of plastic deformation mechanisms and interpretation of strain hardening effects.

Although the origin of the planar glide is attributed to "glide plain softening" in the majority of the studies, the mechanisms leading to this phenomenon are still discussed controversially. The interaction between dislocations and $\varkappa$-carbides during plastic deformation is found to strongly promote this phenomenon. As detailed in [6,7,10,23,24,31,32], the ordered $\varkappa$-carbides first hinder the dislocation movement and are then sheared by preceding dislocations on a single glide plain. As a consequence, this glide plain is softened leading to less resistivity against glide of trailing dislocations. The same mechanism was reported in high-Mn light-weight steels that do not constitute fully ordered $\varkappa$-carbides, rather are characterized by short-range-ordered (SRO) regions in the solid solution state [27,32–34]. In this case, it is assumed that the clusters of SRO are disordered by a gliding dislocation. As a result, the resistance against movement of trailing dislocations is decreased and thus, a specific glide plain is softened.

In addition to the origin of planar glide in high-Mn light-weight steels, the strain hardening response is still a matter of discussion. Hence, similar to the TWIP and TRIP

mechanisms known from HMnS, several new deformation mechanisms such as shear-band induced plasticity (SIP) [6], microband induced plasticity (MBIP) [24], slip-band refinement induced plasticity (SRIP) [23] or dynamic slip band refinement (DSBR) [10] have been introduced. The SIP concept was comprehensively reported by Frommeyer and Brüx [6], who investigated the microstructures and mechanical properties of high-strength Fe-Mn-Al-C light-weight triplex steels. According to their findings, enhanced ductility was promoted by dislocation glide sustained by the uniform arrangement of nano-sized $\varkappa$-carbides coherent to the austenitic matrix. This observation was accompanied by a homogeneous shear-band formation on {111} planes in the austenitic matrix (as shown by the TEM). Based on the MBIP mechanism suggested by Yoo and Park [24], the enhanced strain hardening is explained in terms of the Hall-Petch effect. At low strains, formation of a Taylor lattice (TL) structure was observed. With increasing deformation this is followed by the formation of domain boundaries (DBs) consisting of geometrically necessary dislocations. For further strain accommodation, microbands (MBs) are formed between parallel DBs being characterized by short separation distances. At highest strains, further formation of DBs and MBs and their interaction causes grain subdivision. In contrast to this, Welsch et al. [10] rationalized the strain hardening behavior by DSBR. According to their findings, dislocation sources in the form of Frank-Read sources and grain boundary sources get activated and start to emit dislocations at the onset of plastic deformation. As the generated dislocations do only rarely leave their glide plane (planarity of slip), the glide plane fills up with dislocations. These piled-up dislocations eventually lead to back stresses acting on the source, which increases with the number of emitted dislocations. Once the local stress at the source does not meet the critical activation stress, the source ceases to emit further dislocation loops, thus becomes exhausted. At this point the slip plane is filled with dislocations appearing as slip bands throughout the grain, being fully developed, as the generation of dislocations within the slip band is strongly inhibited. In order to further accommodate plastic strain the generation of more dislocations and thus activation of new sources is necessary. Expanding dislocation loops on their respective glide planes are produced by these sources, which induces the formation of more slip bands leading to a refinement of the slip band substructure. As a consequence, the spacing between the slip bands reduces during straining leading to a strong increase in the stored dislocation density that contributes to strain hardening. This mechanism is in line with the results of Haase et al. [23], who investigated the deformation behavior of a $\varkappa$-carbide-free and $\varkappa$-carbide-containing high-Mn light-weight steel. The authors showed that plastic deformation is governed by planar dislocation glide and slip band formation in all states. Thus, the SRIP effect, which was also

shown in a study by Yao et al. [9], is responsible for the high work-hardening rates observed. Slip band promoted plasticity is further supported by a recent study of Kim et al [26]. Using in-situ transmission electron microscopy (TEM) analysis, the authors revealed that plastic deformation in an austenitic high-Mn light-weight steel is accommodated by pronounced planar dislocation glide followed by the formation of SBs and highly dense dislocation walls (HDDWs). In that study, localized cross-slip of dislocations at slip band intersections was revealed, eventually indicating that the SBs can propagate in a grain without blocking each other [26].

The introduction clearly highlights the complexity of Fe-Mn-Al-C light-weight steels with respect to phase compositions as well as dislocation motion, strain hardening and plastic deformation processes under monotonic load. However, many of the envisaged applications for these steels, e.g. in the mobility sector, will undergo cyclic loading during service life. Thus, in-depth analysis of the cyclic deformation response (CDR) and the fatigue behavior is essential in order to fully understand the deformation behavior of these alloys and to allow for reliable, wide-spread use. At this point, only a few studies available in literature focused on the behavior of high-Mn light-weight steels under cyclic load [35–43]. Anyway, only two of these studies investigated the influence of $\varkappa$-carbides on the fatigue properties. Tjong [42] investigated the low-cycle fatigue behavior of an austenitic Fe-25Mn-8Al-1C alloy aged at 700 °C for 24 h. A high density of coarse x-phase carbides at the austenite grain boundaries as well as fine $\varkappa$-phase carbides within the grains acting as effective barriers to slip dislocations during fatigue, were reported. An inhomogeneous distribution of a high density of intergranular carbide and the formation of planar arrays of dislocations lead to an observed two-slope behavior in the Coffin-Manson relationship. Ho et al. [43] reported on the cyclic softening of age-hardened Fe-Mn-Al-C alloys containing coherent precipitates. In this study, strain-controlled fatigue tests were conducted using a Fe-Mn-Al-C lightweight alloy in differently aged conditions, i.e. 550 °C for 2 h, 550 °C for 24 h and 710 °C for 2 h. Despite of the actual aging parameters, the CDRs of all conditions were characterized by cyclic softening throughout the tests. This softening was explained by the shearing of $\varkappa$-carbides and their depletion within persistent slip bands (PSBs). However, a direct comparison of microstructure evolution of the alloy in focus with and without $\varkappa$-carbides has not been contemplated under fatigue loading in literature so far. Thus, the role of the $\varkappa$-carbides cannot be deduced straightforward as the general deformation behavior under cyclic is not addressed as a baseline for comparison. From the state-of-the-art presented above it is obvious that the fatigue behavior of high-Mn light-weight steels, especially the impact of $\varkappa$-carbides on the properties under cyclic load, needs to be investigated more thoroughly.

In order to close this prevalent research gap, the low-cycle fatigue (LCF) behavior of an austenitic Fe-29.8Mn-7.65Al-1.11C alloy, which differs in chemical composition from all alloys investigated in fatigue studies so far, was investigated thoroughly in present work. Thereby, CDRs of both, a homogenized, fully austenitic condition and an aged, austenitic and ϰ-carbide-containing condition stemming from one initial single batch with the exact identical chemical chemistry were comprehensively studied for the first time. The direct comparison of these conditions provides novel insights into the topic, i.e. the influence of ϰ-carbide precipitates on the behavior of a high-Mn light-weight steel under cyclic load. The results are critically discussed based on microstructural as well as on assessment of evolution of plastic strain amplitude and fracture surface analysis. Besides microstructural characterization by electron back-scatter diffraction (EBSD) for determination of the influence of texture, grain size and grain morphology, synchrotron diffraction experiments were carried out in transmission mode. In contrast to the local phenomena revealed by TEM investigations in literature [37,42,43], statistically confirmed volume effects are thus represented by the synchrotron results discussed in the current study. Finally, fatigue life of these alloys is evaluated based on the Coffin-Manson law and Basquin equation.

2. Material and methods

The material investigated in the current study is a Fe-29.8Mn-7.65Al-1.11C steel with a SFE of ~ 85 mJ/m^2 [23]. The exact chemical composition is given in Table 1 [23]. The steel was provided as strip cast sheets with a thickness of 1.6 mm.

Table 1 Chemical composition of the investigated Fe-29.8Mn-7.65Al-1.11C steel (in wt.%) [23].

Element	Fe	Mn	Al	Si	C	S	N
wt.%	Bal.	29.8	7.65	0.0093	1.11	0.017	0.0083

After strip casting the sheets were homogenized and additionally cold rolled up to 30 % thickness reduction. For microstructure analysis and mechanical characterization flat dog-bone shaped specimens with a nominal gauge section of 8 mm × 3 mm × 1.6 mm (displayed in Fig. 1b) were cut from the sheets by electro-discharge machining (EDM). The loading direction (LD) of the specimens corresponds to the rolling direction (RD) of the sheets. According to [23] and as schematically shown in Fig. 1a), the specimens were subjected to different heat-treatments upon EDM in order to achieve different microstructural conditions, i.e. a fully austenitic single phase- as well as an aged dual phase-condition consisting of austenite and ϰ-

carbides. These conditions are denoted as condition A and B, respectively, in the reminder of this article. For further information on the heat-treatments performed and on the determination of annealing parameters by CALPHAD-based, thermodynamic calculations the reader is referred to [23].

In order to guarantee a high surface quality, all specimens were mechanically ground to 5 μm grit size using SiC paper after heat-treatment. Microstructure analysis as well as post-fatigue fracture surface analysis were carried out using a Zeiss ULTRA GEMINI high-resolution SEM operating at 30 kV. The SEM system is equipped with an electron back-scatter diffraction (EBSD) unit. For EBSD measurements specimens were further vibration polished for 12 h using conventional oxide polishing suspension (OPS) with a grain size of 0.04 μm. All measurements were performed at the same working distance, magnification and step size, i.e., 15 mm, 100× and 1.5 μm. Bruker Esprit software was used for data post-processing, i.e. determination of austenite grain size and removal of non-indexed points, taking at least five neighboring points into account.

For further microstructure analysis, synchrotron diffraction experiments were carried out at the side station of the P07-material science beamline, at the storage ring PETRA III at DESY in Hamburg [44]. The specimens were measured in transmission mode using an X-Ray energy of 87.1 keV and a Perkin Elmer XRD 1621 image plate detector with a sample to detector distance of 988 mm. The specimen were scanned along LD with a spot size of 1×1 mm² and an exposure times of 0.2 s and 0.1 s.
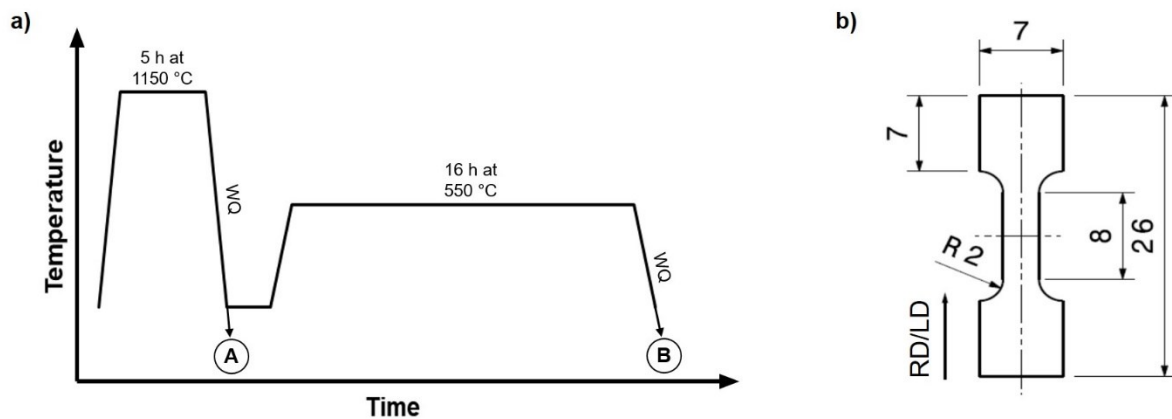

Figure 1: *a) Schematic representation of the heat treatment process considered in present work in order to establish the material in states A (homogenized) and B (aged); b) geometry of tensile and fatigue specimens.*

Vickers hardness testing was conducted on a Struers DuraScan-70 system employing a load of 9.81 N. Uniaxial room temperature tensile tests were performed using a screw-driven MTS Criterion load frame with a maximum loading capability of 20 kN under displacement

control with a constant crosshead speed of 2 mm/min. Nominal stress-strain diagrams were plotted based on load and displacement signals as well as gauge section dimensions depicted in Fig. 1b). LCF experiments were conducted at ambient temperature using a digitally controlled servo-hydraulic load frame with a maximum force of 16 kN. For accurate strain measurement a MTS miniature extensometer featuring a gauge length of 5 mm was directly attached to the surface of the specimens. The LCF tests were carried out in fully reversed push-pull loading ($R\varepsilon = -1$) in total strain control with a constant strain rate of 6×10^{-3} s^{-1} and total strain amplitudes of $\Delta\varepsilon_t/2 = \pm 0.2\%$, $\Delta\varepsilon_t/2 = \pm 0.4\%$ and $\Delta\varepsilon_t/2 = \pm 0.6\%$.

3. Results and discussion

Microstructural analysis after different heat treatments was carried out by EBSD. Fig. 2 a) and b) shows representative EBSD inverse pole figure (IPF) maps with superimposed image quality for both conditions, A and B. Histograms of the grain diameters and grain boundary misorientation angles directly obtained from the EBSD micrographs shown in a) and b) are represented in c) and d) as well as e) and f), respectively. Irrespective of the heat treatment, similar microstructures can be observed with respect to grain morphology and crystal orientation. Both conditions reveal a high fraction of recrystallization twins embedded in a non-textured microstructure. As can be seen, except of one larger grain for condition A, respectively two for conditions B, both conditions are characterized by a similar, relatively homogeneous microstructure with respect to grain size distribution, eventually revealing a bimodal microstructure dominated by the fine grained fraction with an average grain size of approximately 65 μm. This kind of microstructure and weak crystallographic texture, respectively, are a result of primary recrystallization occurring during homogenization annealing of the cold-rolled sheet, as has been reported previously for high-Mn steels [7,45,46]. As expected and in line with the results shown by Haase et al. [23], the aging process did not change the microstructure with respect to grain size, grain boundary character (cf. Fig. 2 e) and f)) and texture. Thus, an effect of grain size on the mechanical properties, as demonstrated for cold-rolled material after homogenization in [23], especially on the LCF behavior is excluded in present work. Eventually, this allows for interpretation of the influence of ϰ-carbides exclusively.
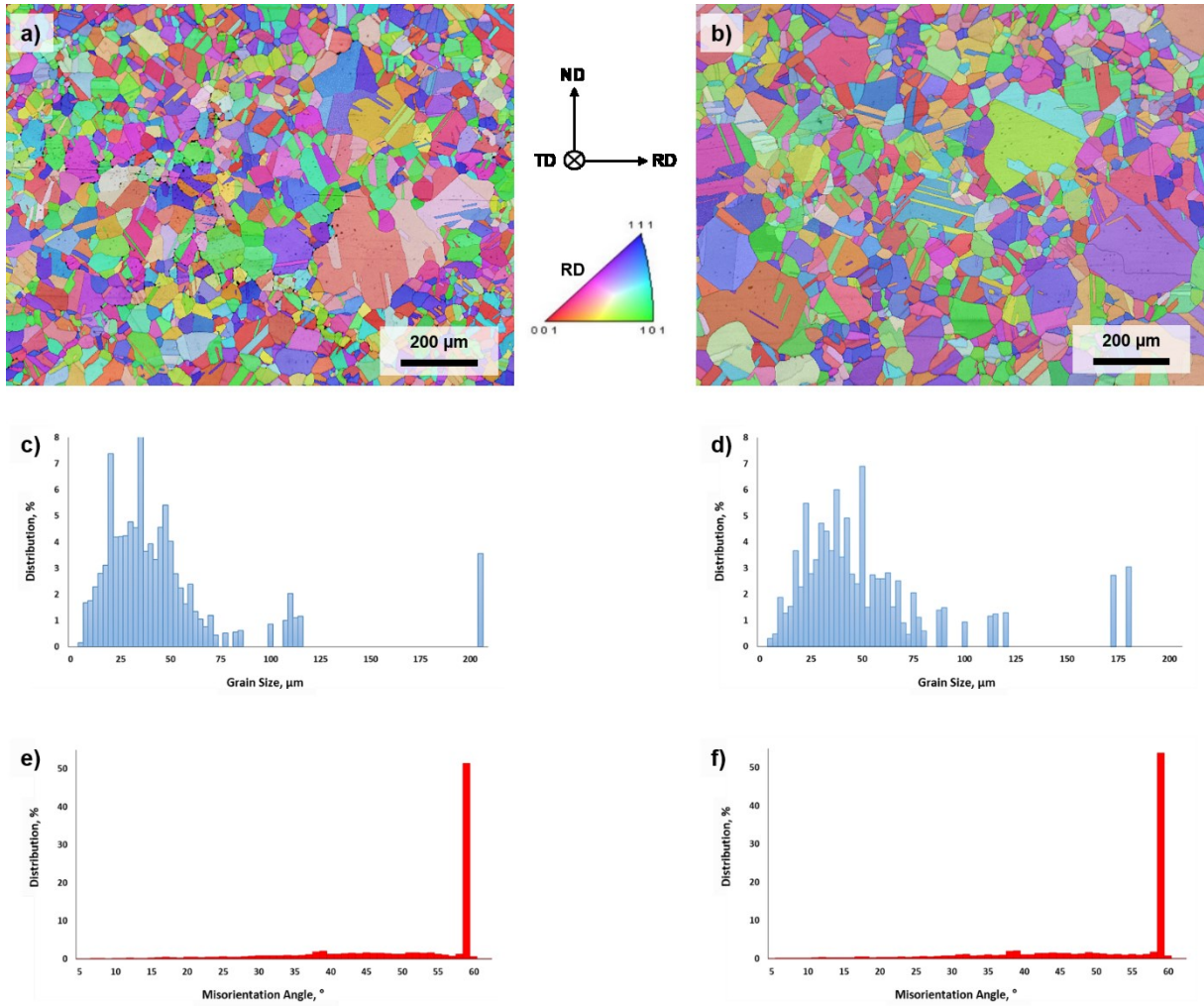
Figure 2: *EBSD inverse pole figure maps with superimposed image quality of a) condition A (homogenized) and b) condition B (aged). The grain orientations are plotted with respect to the rolling / loading direction. Histograms of the grain diameters and grain boundary misorientation angles of the EBSD micrographs shown in a) and b) are represented in c)-d) and e)-f), respectively.*

Figure 3 shows synchrotron diffractograms of the homogenized (a) and aged (c) condition, respectively. In order to separate the peaks of the ϰ-carbides from background noise more clearly, an exposure time of 0.1 s for each of three integrated detector pictures for condition B (Fig 3b) as compared to 0.2 s using a single detector picture for condition A (Fig. 3a) was used, resulting in higher intensity amplitude as shown in Fig. 3. For evaluation of data, 4 diffraction peaks of the austenitic phase, corresponding to the 100, 111, 200 and 400 hkl plane were fitted based on the summation of three different Gaussian functions. This approach was chosen to fit and analyze data considering the overlapping of three diffraction peaks. For further details on this approach in comparison to other well-established techniques readers are referred to [47]. For the sake of brevity the evaluation procedure only is highlighted exemplarily in Fig. 3 e) and f). Magnified views of the respective diffraction profile from the 400 hkl lattice plane of both conditions (marked by red rectangles in Fig. 3 a) and b)) are depicted in Fig. 3 c) and d). At the first glance, the diffractogram of the homogenized condition A in 3 a) shows a fully

austenitic microstructure as deduced from the presence of only γ-peaks. In contrast, the presence of ϰ-carbides is proven by the asymmetric peak-broadening revealed by the pattern of the aged condition B displayed in Fig. 3 b). The peak-broadening, as shown in literature [23,48–50], becomes even more obvious in the magnified depiction of the peak of the 400 hkl lattice plane condition B in Fig. 3 d). Thus, in contrast to the local evidence of ϰ-carbides as shown by TEM in literature, statistically confirmed volume effects are represented by the synchrotron transmission mode experiments. According to the results revealed by Choo et al. [49], and as schematically shown in the work of Kalashnikov et al. [48], the evolution of the diffractograms can be explained by the spinodal decomposition of the ϰ-carbide particles and concomitant formation of side-bands. The formation of ϰ-carbides, these being characterized by an increased lattice parameter as compared to the γ-matrix, causes asymmetric peak-broadening to lower 2Θ-angles. In parallel, depletion of interstitial carbon and possibly substitutional aluminum atoms in the γ-matrix, marked by the arrow γ_0 in Fig. 3 d), results in side-band formation at higher 2Θ angles. The formation of the ϰ-carbides in condition B is further underlined by the Gaussian peak-fit for the 400 hkl peak detailed in Fig. 3 f). Based on the consideration of 3 peaks (visualized by the green curves), the best possible fit (being characterized by an error of the sum spectrum to the measured value of 1.746% as well as a coefficient of determination (R^2) of 0.99569) was obtained. As for condition B of the current study there are no differences with respect to chemical composition, material state and heat treatment parameters are prevailing compared to [23], it can be assumed that nanosized ϰ-carbide precipitates were distributed homogeneously and share a coherent interface with the austenitic matrix. From the magnified view of the 400 hkl peak of the non-aged condition A presented in Figure 3 e) minor formation of side-bands caused by spinodal decomposition can also be deduced. This is in line with the corresponding results of the Gaussian peak profile-fit shown in Figure 3 e), as the best fit was obtained for 3 peaks with an error and R^2-value of 0.865% and 0.99871, respectively. These results are supported by the findings of Song et al. [51], who investigated the ϰ-phase formation in Fe–Mn–Al–C austenitic steels. The authors demonstrated, also via synchrotron measurements, that the formation of nano-sized clusters/ϰ-carbides already occurred after quenching from the austenitic phase of a Fe-30Mn-8Al-1.2C steel. This, however, could not be detected by macro-XRD measurements by Haase et al [23]. Thus, it has to be assumed that minor volume fractions of clusters/ ϰ-carbide precipitates are already present in the homogenized condition A of the current study. However, these fractions are well below fractions being reported in case of fatigue studies being available in literature so far [43] and, eventually, assumed to not significantly contribute to the elementary mechanisms being in focus

of present work as will be discussed in the remainder of this paper. Here, this condition is referred to as ϰ-carbide free.
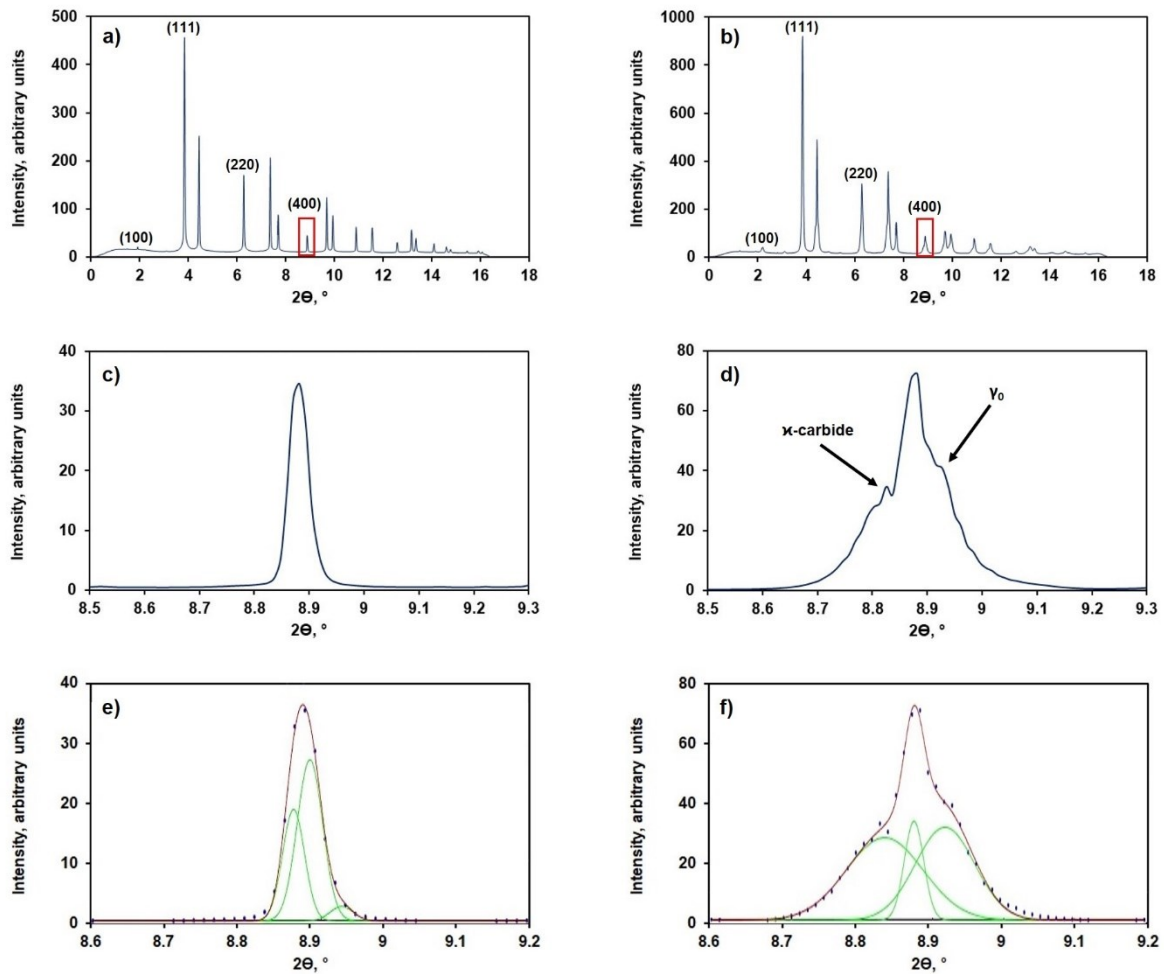

Figure 3: *Synchrotron X-ray diffractograms of the a) homogenized and c) aged condition; b) and d) show magnified details of 400hkl plane diffraction peaks marked in the red rectangles in a) and c); e) and f) depict Gaussian peak-fits of the 400hkl plane diffraction peaks revealing the presence of ϰ-carbides even after homogenization.*

Figure 4 shows hardness maps of the homogenized condition A and aged condition B, respectively. The measurements were carried out over the full length (i.e., gauge length and grip section of the specimen shown in Fig. 1b)) in order to analyze the overall homogeneity of the hardness after heat treatment. In total 451 individual measurements were carried out. From the hardness map of condition A displayed in Fig. 4 a), a homogeneous hardness distribution with a mean value of 245 HV 0.2 and a standard deviation of 9.3 HV 0.2 is observed. The maximum and minimum value were determined as 271 HV 0.2 and 218 HV 0.2, respectively. The effect of age-hardening can be derived from the hardness map of condition B displayed in Fig 4 b). The mean hardness value increased to 398 HV 0.2. Maximum and minimum values as well as standard deviation were determined as 447 HV 0.2, 335 HV 0.2 and 17.7 HV 0.2, respectively. Thus, the hardness of the Fe-29.8Mn-7.65Al-1.11C steel investigated can be

increased by a factor of ~ 1.5 due to $\varkappa$-phase precipitation. The increase in hardness corresponds well with results reporting on similar compositions and aging treatments, e.g. reported in [52].
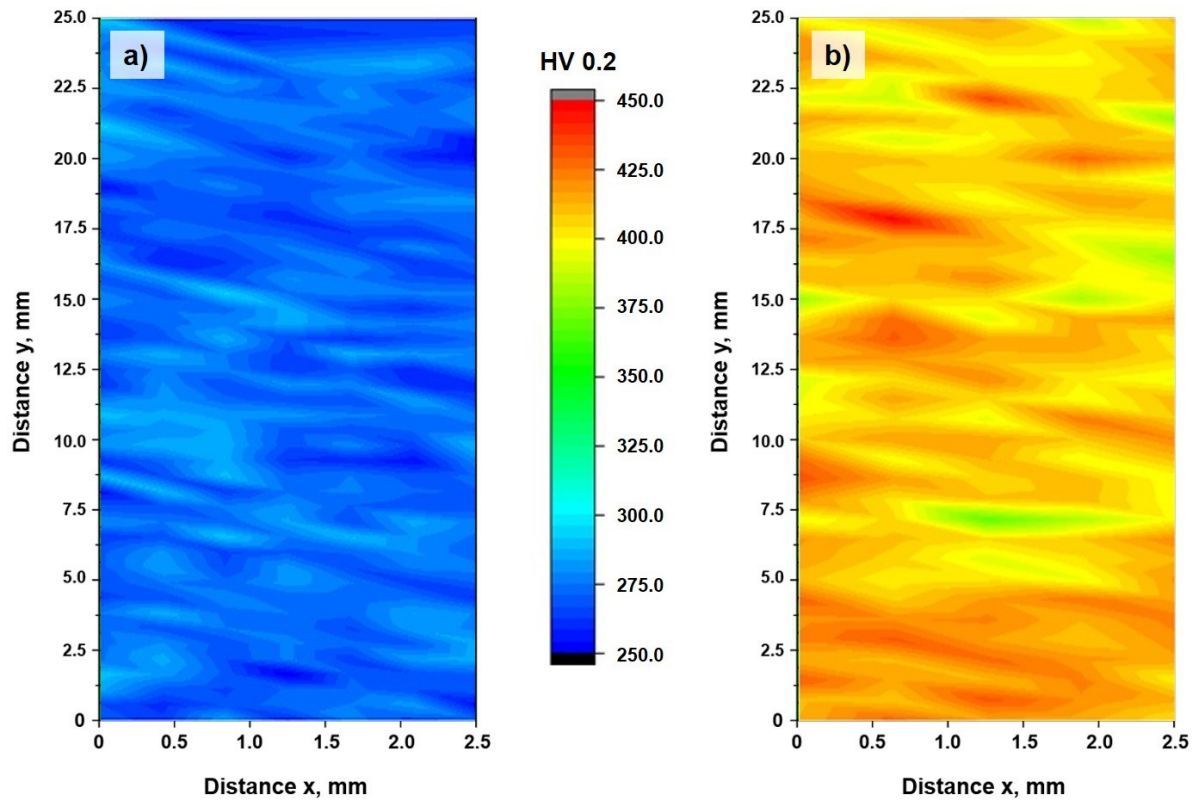

Figure 4: *Hardness maps (HV0.2) showing the hardness distribution over the entire area of a) the homogenized (b) the aged specimen. Distances in x and y are representing the RD/LD and the ND of the specimen, respectively.*

The behavior under monotonic tensile loading, shown in Fig. 5, is illustrated by representative stress-strain curves obtained for both conditions considered, i.e. condition A and condition B. The homogenized condition A is characterized by a yield strength (YS), ultimate tensile strength (UTS) and elongation to failure of approximately 375 MPa, 845 MPa and 59%, respectively. Compared with condition A, an increase in YS and UTS up to ~ 850 MPa and 1040 MPa with a concomitant decrease of ductility to 39% can be observed as a result of the aging treatment. Regarding strength und ductility, the results shown are in line with tensile properties numerously published in literature for similar compositions and aging heat treatments [7,13,21,22,30]. According to Haase et al. [23], the high work-hardening rates and ductility of the conditions shown can be attributed to the SRIP. Glide plain softening, caused by interaction between dislocations and short-range order/ long-range order (SRO/LRO) clusters in the homogenized as well as dislocations-$\varkappa$-carbides interaction in the aged SRIP steel, were revealed as well [23].
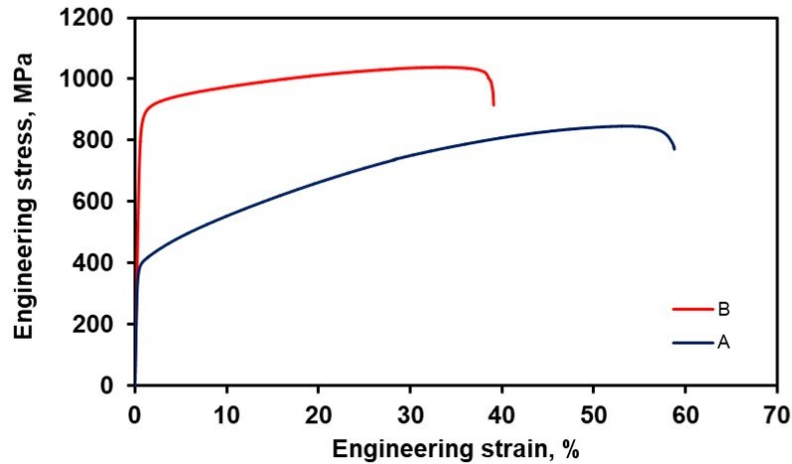
Figure 5: *Tensile stress-strain curves for representative specimens of the investigated Fe-29.8Mn-7.65Al-1.11C steel in homogenized (A) and aged (B) condition.*

Figure 6 displays the CDR of the Fe-29.8Mn-7.65Al-1.11C light-weight steel for both conditions considered. Tests were conducted at various total strain amplitudes, i.e., $\Delta\varepsilon_t/2 = \pm$ 0.2% (a), $\Delta\varepsilon_t/2 = \pm 0.4\%$ (b) and $\Delta\varepsilon_t/2 = \pm 0.6\%$ (c). For each condition and strain amplitude at least three tests have been carried out to analyze the reproducibility and scatter behavior of the LCF response. Since no pronounced scatter was observed with respect to resulting stress amplitudes and number of cycles to failure, only the curves from one test under given loading conditions are shown for sake of brevity. It has to be noted that the load was increased stepwise during the first cycles in order to avoid buckling of the specimens. Consequently, the prescribed strain amplitude was reached after approximately 10 cycles, depending on the actual strain amplitude. Thus, these initial cycles were not taken into account for evaluation and data are shown only starting from the 11th cycle. This approach was adopted from another recently published study [53]. As a common feature of both conditions, the stress amplitude increases and the lifetime decreases with increasing strain amplitude. Irrespective of the strain amplitude and in line with the results from tensile testing, higher stress levels can be derived for condition B, as a result of the higher initial yield strength promoted by precipitation hardening. The CDRs of the homogenized condition are characterized by similar courses for all total strain amplitudes considered, i.e. initial cyclic softening (prevailing for a higher number of cycles for the lower total strain amplitudes) is followed by a saturation stage prior to failure. The initial cyclic softening presumably results from rearrangement of dislocations and a decrease in the overall dislocation density, respectively. This behavior, also similarly shown by Niendorf et al. [54], was explained by Lambers et al. [55] investigating the influence of pre-straining on the low-cycle fatigue response of an austenitic Fe61Mn24Ni6.5Cr8.5 alloy. In this study a decrease in dislocation density and moreover a rearrangement of dislocations into cells was shown for

conditions with CDRs being characterized by cyclic softening. In contrast, pronounced differences are seen in case of the CDRs of the aged condition B. While a stable stress plateau with no initial hardening or softening can be seen for the lowest total strain amplitude of $\Delta\varepsilon_t/2$ $= \pm\, 0.2\%$ (cf. Fig. 6 a)), cyclic softening occurs at the medium and highest total strain amplitude, being even more pronounced for the latter. Accordingly, differences in number of cycles to failure become obvious by comparing both conditions. While fatigue life at the lowest total strain amplitude considered for condition B, i.e. about 170.000 cycles, is more than twice higher than for condition A ($\sim$ 80.000 cycles), this trend changes upon the onset of cyclic softening of the aged condition, i.e. when the strain amplitude increases. An almost similar number of cycles to failure of approximately 13.000 cycles is revealed for the medium total strain amplitude for both conditions, whereas for the highest total strain amplitude of $\Delta\varepsilon_t/2 = \pm\, 0.6\%$, the fatigue life of the homogenized condition A is, with $\approx$ 4.500 cycles, five times higher than that of the aged counterpart ($\approx$ 900 cycles). The cyclic deformation behavior of both conditions becomes more apparent upon evaluation of the plastic strain range development, as shown in Fig. 7. It has to be noted that, in order to exclude strain ramping effects from analysis, every 25th hysteresis loop was recorded only starting at cycle 100. Thus, development of the plastic strain range is plotted starting from the 100th cycle in Fig. 7. For condition A it is seen from Fig. 7 a) that, as the total strain amplitude increases, the plastic strain range is also characterized by a steady increase. In line with the CDRs presented, cyclic saturation can be derived, since the plastic strain range remains unchanged throughout the tests. In contrast, differences in the development of plastic strain ranges are obvious for condition B displayed in Fig. 7 b). At the lowest total strain amplitude of $\Delta\varepsilon_t/2 = \pm\, 0.2\%$, a constant level of plastic strain, virtually equal to zero (indicating a fully elastic cyclic behavior) can be seen. Upon increasing $\Delta\varepsilon_t/2$, a steady increase of the plastic strain range is evidenced by Fig. 7 b). From this observation it can be deduced that cyclic softening of the aged condition in case of the medium and highest total strain amplitude, as revealed by the CDRs, is triggered by the onset of (cyclic) plasticity.
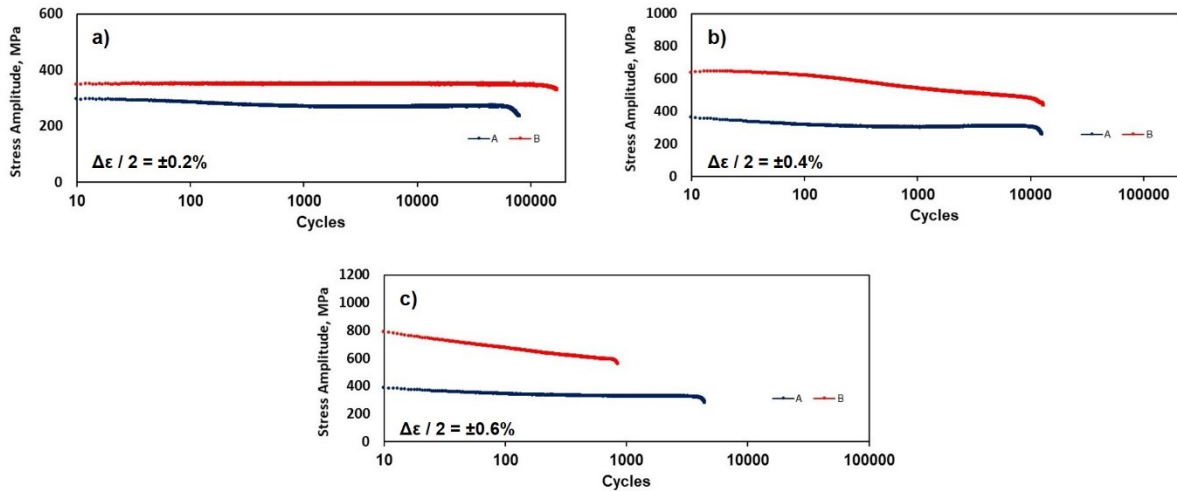
Figure 6: *Cyclic stress response at room temperature at total strain amplitudes of a) $\Delta\varepsilon_t/2 = \pm 0.2\%$, b) $\Delta\varepsilon_t/2 = \pm 0.4\%$ and $\Delta\varepsilon_t/2 = \pm 0.6\%$ (c) for Fe-29.8Mn-7.65Al-1.11C steel in homogenized (A) and aged (B) condition.*
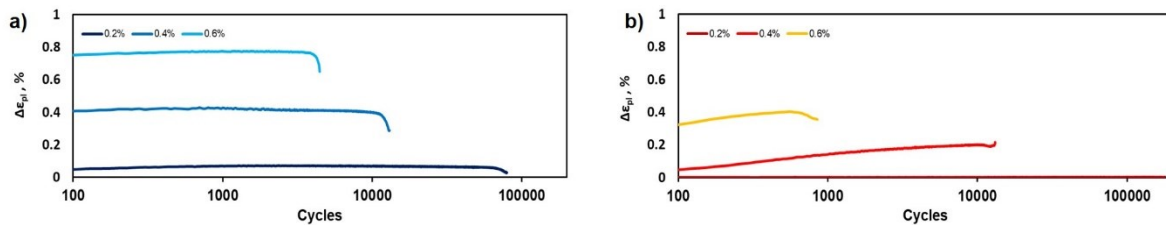

Figure 7: *Cyclic plastic strain response in homogenized (a) and aged (b) conditions at the total strain amplitudes of $\Delta\varepsilon_t/2 = \pm 0.2\%$, $\Delta\varepsilon_t/2 = \pm 0.4\%$ and $\Delta\varepsilon_t/2 = \pm 0.6\%$.*

The results of the plastic strain range development are in perfect agreement with the comparison of half-life hysteresis loops depicted in Fig. 8 a-c. Irrespective of the total strain amplitude, wide-opened hysteresis loops can be seen for the homogenized condition, whereas contribution of plastic strain for the aged condition can only be derived for the medium and highest strain amplitude. For the lowest total strain amplitude of $\Delta\varepsilon_t/2 = \pm 0.2\%$, condition B is characterized by a fully elastic behavior without any sign of plastic strain as deduced from the completely closed half-life hysteresis loop.

Half-life hysteresis loops plotted in relative coordinates for conditions A and B are shown in Fig. 8 d) and e), respectively. The upper branches of the hysteresis loops of the aged samples (cf. Fig. 8 e)) are congruent indicating almost perfect Masing behavior. Thus, very similar microstructure evolution independent of the strain amplitude imposed can be deduced for the ϰ-carbide-containing aged condition [53,56,57]. In contrast, congruence of the upper branches of the hysteresis loop for condition A is only revealed for the medium and highest total strain amplitude. As a consequence, significant variations can be expected between microstructure evolution at these total strain amplitudes and $\Delta\varepsilon_t/2 = \pm 0.2\%$. In a study reporting on the cyclic stress-strain behavior of an austenitic Fe-29.7Mn-8.7Al-1.04C alloy at room

temperature, Ho and Tjong [38] revealed the formation of κ-carbides upon cyclic loading at high strain amplitudes. The authors concluded that the κ-phase carbides, nucleated in the matrix during initial cycling at high strain amplitude, re-dissolved within persistent slip bands (PSBs) because of dissolution or disordering of the precipitates by the motion of dislocations in the PSBs. However, experimental proof is missing and will be subject of future work. From these results carbide formation in condition A of the present study fatigued at medium and high strain amplitudes can be presumed, eventually rationalizing the non-Masing behavior. Obviously, a complex interplay of various mechanisms contributes to the overall microstructural evolution leading to different conclusions depending on the trend lines assessed, i.e. stress response, plastic strain response and Masing behavior (when evaluated and compared separately). Further studies will be needed to separate each individual contribution and to eventually get a deeper understanding of the complexly interacting phenomena.
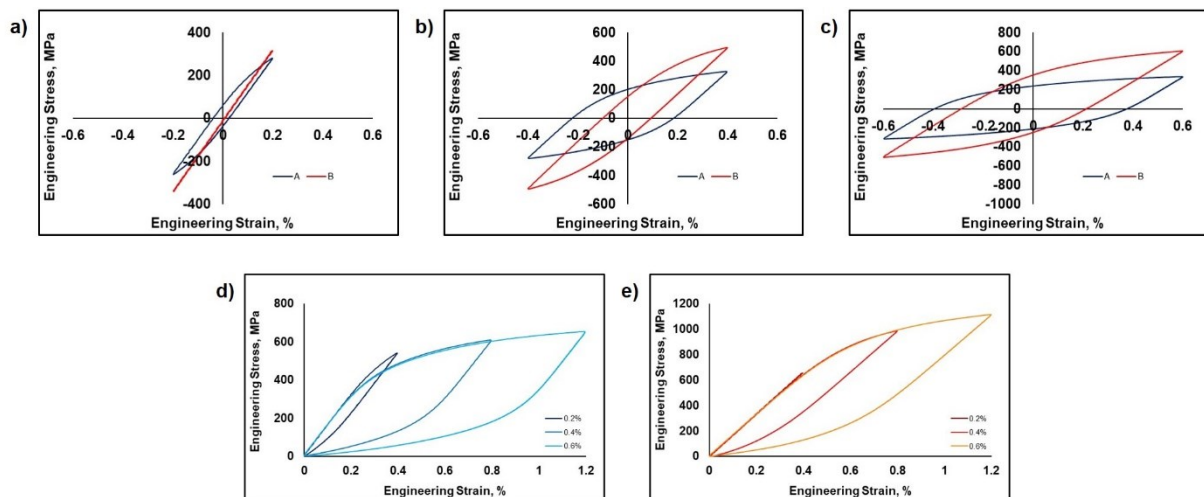

Figure 8: *Half-life hysteresis loops for the Fe-29.8Mn-7.65Al-1.11C steel in homogenized (A) and aged (B) conditions for total strain amplitudes of (a) Δεₜ/2 = ± 0.2%, (b) Δεₜ/2 = ± 0.4% and (c) Δεₜ/2 = ± 0.6%; Half-life hysteresis loops plotted in relative coordinates for d) condition A and e) condition B.*

Ho et al. [43] reported cyclic softening of a κ-carbide-containing Fe-29.7Mn-8.7Al-1C alloy aged at different temperature-time conditions. The results were similar to the ones reported in the present study. The authors showed that cyclic softening was, i.a., associated with shearing of κ-carbides and mechanical dissolution of the precipitates. In order to explain the CDRs of the aged condition B of the present study, post-fatigue synchrotron analysis was conducted for the specimen fatigued at the highest total strain amplitude of Δεₜ/2 = ± 0.6%. The results (focusing on the diffraction peak of the 400 hkl plane) highlighted by the Gaussian peak-fit are illustrated in Fig. 9 a) and b), respectively. To allow for direct comparison and critical assessment of the differences before and after fatigue, the peak of the non-deformed condition already plotted in Figure 3 d) (depicted by the dashed line) is recompiled in Figure 9 a).

Compared to the 400 hkl diffraction peak of the non-deformed condition, the peak profile changes as a result of fatigue loading. On the one hand, both side peaks representing the formation of ϰ-carbides at lower and depletion of the surrounding matrix at higher 2Θ-angles are almost vanished. In line with the results of Ho et al. [43], this clearly indicates that shearing (decrease of intensity of the ϰ-side band) and dissolution (decrease of intensity of the side band of γ_0) of the precipitates are the most important factors contributing to cyclic softening during fatigue at higher strain amplitudes. Further changes upon cyclic loading are demonstrated by the Gaussian peak fit shown in Fig. 9 b). As a result of fatigue loading, the area of both side band peaks was reduced by approximately 85%. On the other hand, the high amount of plastic deformation can be derived from the increased width of the austenite γ-peak (approximately 400%). It is well-known that defects induced by plastic deformation deteriorate the perfection of the crystal lattice. As a result, the amplitude and symmetry of the peaks in XRD experiments is decreased upon plastic deformation, whereas their half-width is increased (while the peak center may be shifted) [58]. This phenomenon was amongst others shown by Scott el al. [59], who investigated the impact of precipitation strengthening in high-Mn austenitic TWIP steels. As mentioned before, in present work the width of the 400 peak being in focus was increased by 400%, whereas the intensity was decreased by a factor of approximately 2.
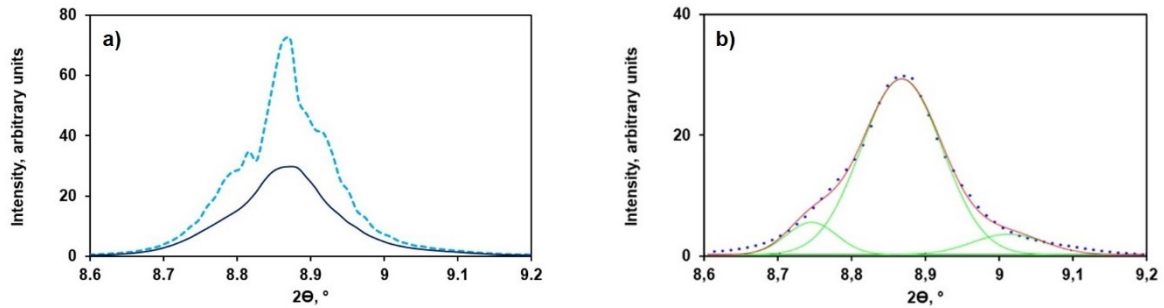

Figure 9: *Synchrotron X-ray diffractogram of the (400) diffraction peak and b) Gaussian peak-fit of the (400) diffraction peak of the aged condition fatigued at a total strain amplitude of $\Delta\varepsilon_t/2 = \pm 0.6\%$ ($N_f = 853$ cycles). As a reference, the (400) diffraction peak of the non-deformed condition is shown in a) (dashed line).*

So far the fatigue performance of the Fe-Mn-Al-C light-weight steel was assessed based on analysis of CDRs, evolution of plastic strain amplitude and half-life hysteresis loops. Moreover, the fatigue properties of a material can be described by the Basquin-Coffin-Manson relationship [60,61]. According to this relation, the total strain amplitude can be separated into two parts, i.e. elastic strain amplitude and plastic strain amplitude, as given by equation (1):

$$\frac{\Delta\varepsilon_t}{2} = \frac{\Delta\varepsilon_e}{2} + \frac{\Delta\varepsilon_p}{2} = \frac{\sigma'_f(2N_f)^b}{E} + \varepsilon'_f(2N_f)^c \qquad \textbf{(1)}$$

where E is the Young's modulus (160 GPa as determined from hysteresis curves in present work), $2N_f$ the number of cycles to failure, σ'_f the fatigue strength coefficient, ε'_f the fatigue ductility coefficient, b the fatigue strength exponent and c the fatigue ductility exponent. The relation between stress amplitude and plastic strain can be calculated based on the following power-law equation (2) [62]:

$$\frac{\Delta\sigma}{2} = K'(\frac{\Delta\varepsilon_p}{2})^{n'}$$

(2)

where $\frac{\Delta\sigma}{2}$ is the half-life stress amplitude, $\frac{\Delta\varepsilon_p}{2}$ the half-life plastic strain amplitude, K' the cyclic strength coefficient and n' the cyclic strain-hardening exponent. Figure 10 displays total strain, plastic strain and elastic strain amplitudes as a function of the number of cycles to failure $2N_f$ in a double logarithmic plot for the homogenized (a) and aged condition (b), respectively. For evaluation of data, half-life stresses and strains were considered to guarantee that cyclic saturation already occurred. The point of intersection $(2N_t)$ for the curves being representative for the elastic and plastic strain amplitudes, is found to be present at 21.380 cycles for condition A and 1.080 cycles for condition B as deduced from Fig. 10 a) and b), respectively. For these numbers of reversals the corresponding total strain amplitude values can be calculated as 0.42% (A) and 0.65% (B) based on data obtained in present work (corresponding trend lines plotted in Fig. 10 as well). Thus, it can be deduced that, with regard to the homogenized condition, a change of elementary mechanisms contributing to damage and failure sets in for total strain amplitudes > ± 0.42%. In contrast, this change of contributing mechanisms only is found for total strain amplitudes > ± 0.65% in the aged condition B. These results give another explanation to the results deduced from Fig. 8 d) and e): almost perfect Masing behavior was observed for condition B, while non-Masing behavior with the upper branches of hysteresis loops only being congruent for strain amplitudes ≥ 0.4% was observed for condition A. Figure 10 c) shows a plot of the half-life stress amplitude as a function of the half-life plastic strain amplitude for both conditions considered. According to equation (2), the values of the cyclic strength coefficient K' and the cyclic strain-hardening exponent n' were determined using the method of least squares. These values, in combination with the coefficients obtained from equation (1), are summarized in Table 2 for both conditions studied, forming an initial basis for the evaluation of fatigue properties of the high-Mn light-weight steel in focus. A different two-slope behavior in the Coffin-Manson relationship accompanied by different low-cycle fatigue

parameters has been shown by Tjong [42]. However, as the chemical composition of the material in focus as well as heat treatment parameters were different compared to the current study. Thus, it can be assumed that even slight differences in composition and/or heat treatment can result in completely different microstructural states and as a result major differences in the fatigue properties of light-weight HMnS. The results of the currents study are additionally recapitulated by the strain-life fatigue data as shown in Fig. 10 d). At high total strain amplitudes superior fatigue strength is revealed for the homogenized condition A as a result of the stable stress response shown (cf. Fig. 6). With decreasing $\Delta\varepsilon_t/2$ this behavior changes, as can be determined from the intersection point of the strain-life curves of both conditions. This is due to the fully elastic deformation of the $\varkappa$-carbide-containing condition B at lowest strain amplitudes. The results of the present study already indicate that a significant improvement of the cyclic properties in the high-cycle fatigue (HCF) regime, which is known to be dominated by crack initiation and failure mainly due to elastic deformation [63,64], by $\varkappa$-carbide precipitation hardening can be expected.
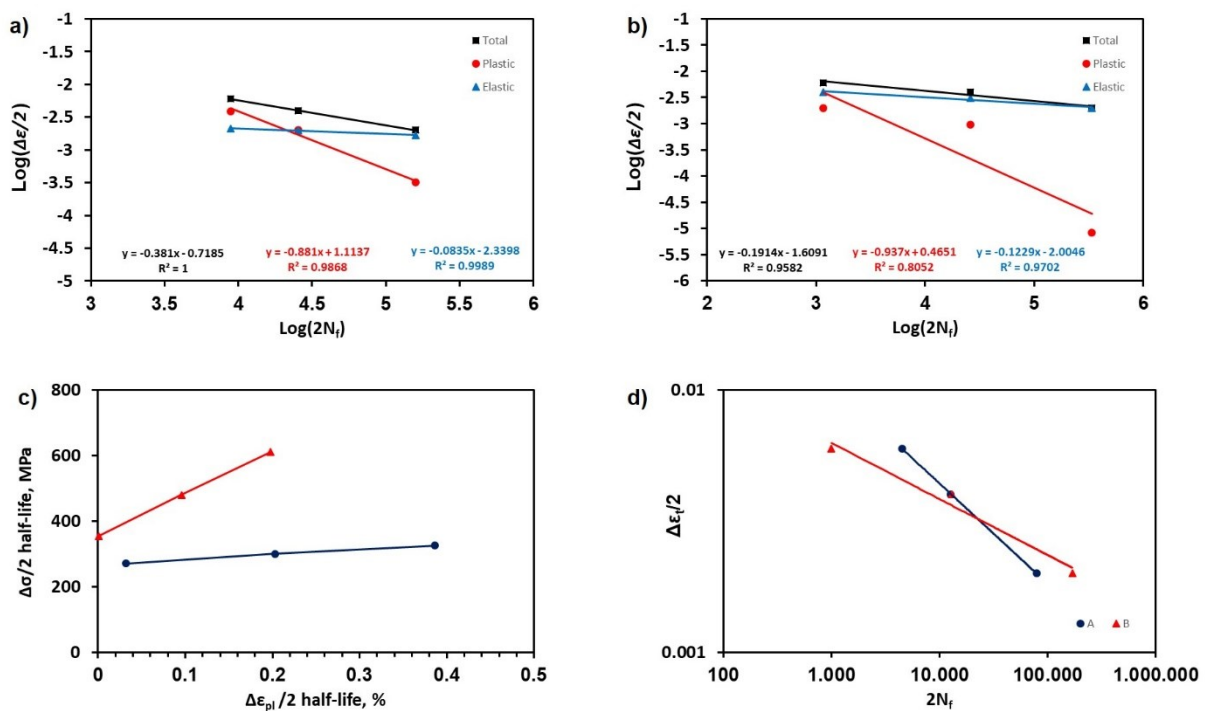

Figure 10: *Cyclic total strain, plastic strain, and elastic strain amplitude-fatigue life response for the Fe-29.8Mn-7.65Al-1.11C steel in a) homogenized and (b) aged condition; c) plastic strain– stress relationship and d) total strain-life fatigue data for both conditions considered.*

Table 2 *Low-cycle fatigue parameters obtained for the Fe-29.8Mn-7.65Al-1.11C steel in homogenized and aged conditions.*

	Low-Cycle Fatigue Parameters						
Condition	K', MPa	n'	σ'_f, MPa	b	ε'_f	c	$2N_t$
A	300.85	0.07	731.68	-0.08	12.99	-0.88	21380
B	659.44	0.09	1583.14	-0.12	2.92	-0.94	1080

Fracture surface analysis was carried out for all specimens tested. The results obtained for the highest total strain amplitude, i.e., $\Delta\varepsilon_t/2 = \pm 0.6\%$ are shown in Fig. 11 for conditions A (a-d) and B (e-h), respectively. As similar characteristics were revealed for specimens fatigued at other strain levels in case of both conditions, the depicted fracture surfaces can be considered as representative. From the pictures shown, well-known features for fatigue tested specimen, i.e., areas of fatigue crack initiation and propagation characterized by sub-micron fatigue striations (cf. Fig. 10 (b), and (f)), as well as an overload final fracture region, characterized by a ductile, dimple-like structure (cf. Fig. 10 (d) and (h)), are seen in case of all specimens and strain amplitudes irrespective of the condition considered. In addition, an increase in the share of the area characterized by stable fatigue crack propagation is observed with a concomitant decrease of the strain amplitude as a result of higher number of cycles to failure (not shown for the sake of brevity). In line with the findings from the tensile tests (data not shown), the fracture surfaces of the fatigued specimen locally seem to be plastically deformed to a high extent. These characteristics can be explained by the very high ductility of both conditions, being most pronounced for the homogenized condition A. In addition, despite of condition and strain level, fatigue cracks basically always initiated from the surface of the specimen. Crack initiation sites of the fracture surfaces shown are marked by the white arrows in (a) and (e). None of the fracture surfaces examined indicated internal crack initiation. The findings deduced from fracture surface analysis clearly indicate that, although pronounced differences in cyclic deformation responses were reported for the conditions considered, damage evolution is well described by similar stages of crack advance.
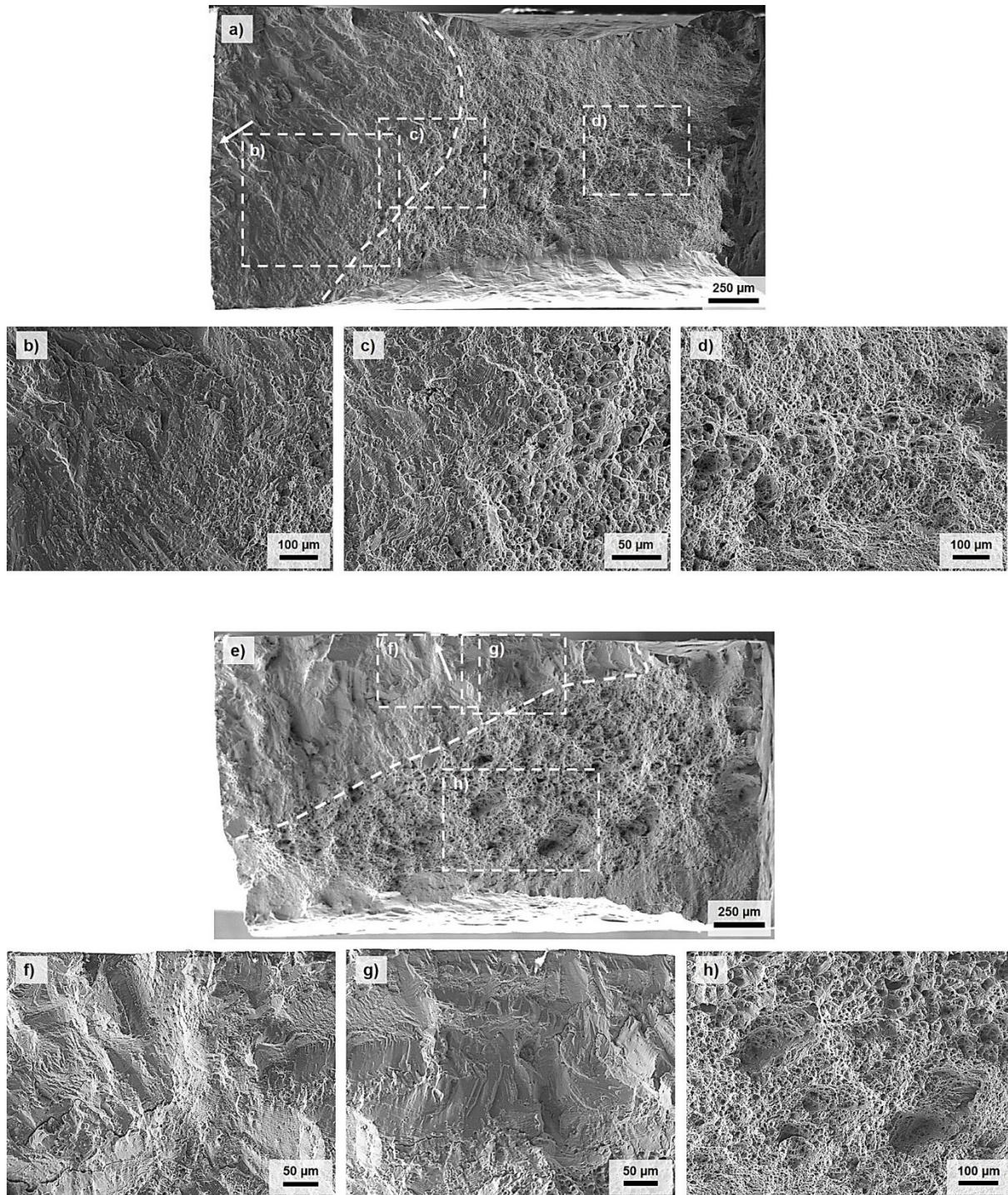
Figure 11: *SEM micrographs of fracture surfaces after fatigue testing at a strain amplitude of $\Delta\varepsilon_t/2 = \pm 0.6\%$ for the Fe-29.8Mn-7.65Al-1.11C steel in (a-d) homogenized and (e-h) aged condition. The subimages (b-d) and (f-h) show magnified views of the marked white dashed rectangles in a) and d). Crack initiation sites are marked by the white arrows in (a) and (e).*

4. Conclusions

Microstructure evolution and mechanical behaviour of a Fe-29.8Mn-7.65Al-1.11C high-Mn light-weight steel under monotonic and particularly strain controlled cyclic loading in the low-cycle fatigue (LCF) regime at room temperature have been investigated. Thereby, two

conditions, i.e., a homogenized austenitic and an aged, $\varkappa$-carbide-containing condition were comprehensively studied. From the findings presented, the following conclusions can be drawn:

- The cyclic deformation response of the homogenized condition (referred to as $\varkappa$-carbide free) is characterized by initial cyclic softening followed by a stress plateau. Upon aging the deformation response is strongly affected.

- For the lowest total strain amplitude considered fatigue properties of the aged condition are improved as a result of $\varkappa$-carbide formation. With increasing strain, cyclic softening is observed for the aged condition resulting in inferior fatigue lifetime as compared to the homogenized specimen.

- Cyclic softening of the aged condition at higher strain amplitudes is rationalized by the onset of plastic deformation as revealed by evaluation of the plastic strain amplitude. Shearing of $\varkappa$-carbides and mechanical dissolution of the precipitates are promoted as evidenced by synchrotron diffraction measurements.

- Similar damage evolution despite different cyclic deformation responses are revealed by fracture surface analysis. Irrespective of the strain level, fractography revealed pronounced ductility as well as fatigue crack initiation from the surface of the specimen.

- Non-Masing behavior in case of the homogenized condition is replaced by almost perfect Masing behavior upon aging. This behavior seems to be contradictory to the evolution of plastic strain in the course of cycling. Obviously, interaction of several elementary mechanisms contributes to the final deformation response of the high-Mn light-weight steel under cyclic loading in the LCF regime.

- In-depth analysis of the fatigue response based on the Coffin–Manson and Basquin equations reveals a change of mechanisms within the interval of strain amplitudes considered. This change of elementary mechanisms eventually contributing to damage initiation and failure is expected to be in line with the aforementioned contradictory behaviors revealed. Futures studies need to be conducted shedding light on the exact nature of the contributing elementary mechanisms and the complex interplay of these mechanisms.

Declaration of interest

Acknowledgements

References

[1] O. Bouaziz, S. Allain, C.P. Scott, P. Cugy, D. Barbier, High manganese austenitic twinning induced plasticity steels, Current Opinion in Solid State and Materials Science 15 (2011) 141–168.

[2] O. Grässel, L. Krüger, G. Frommeyer, L.W. Meyer, High strength Fe–Mn–(Al, Si) TRIP/TWIP steels development — properties — application, International Journal of Plasticity 16 (2000) 1391–1409.

[3] S. Allain, J.-P. Chateau, O. Bouaziz, S. Migot, N. Guelton, Correlations between the calculated stacking fault energy and the plasticity mechanisms in Fe–Mn–C alloys, Materials Science and Engineering: A 387-389 (2004) 158–162.

[4] K. Sato, M. Ichinose, Y. Hirotsu, Y. Inoue, Effects of deformation induced phase transformation and twinning on the mechanical properties of austenitic Fe-Mn-Al alloys, ISIJ International 29 (1989) 868–877.

[5] W. Bleck, C. Haase, Physical Metallurgy of High Manganese Steels, Metals 9 (2019) 1053.

[6] G. Frommeyer, U. Brüx, Microstructures and Mechanical Properties of High-Strength Fe-Mn-Al-C Light-Weight TRIPLEX Steels, steel research international 77 (2006) 627–633.

[7] S. Chen, R. Rana, A. Haldar, R.K. Ray, Current state of Fe-Mn-Al-C low density steels, Progress in Materials Science 89 (2017) 345–391.

[8] H. Kim, D.-W. Suh, N.J. Kim, Fe-Al-Mn-C lightweight structural alloys, Science and technology of advanced materials 14 (2013) 14205.

[9] M.J. Yao, E. Welsch, D. Ponge, S.M.H. Haghighat, S. Sandlöbes, P. Choi, M. Herbig et al., Strengthening and strain hardening mechanisms in a precipitation-hardened high-Mn lightweight steel, Acta Materialia 140 (2017) 258–273.

[10] E. Welsch, D. Ponge, S.M. Hafez Haghighat, S. Sandlöbes, P. Choi, M. Herbig, S. Zaefferer et al., Strain hardening by dynamic slip band refinement in a high-Mn lightweight steel, Acta Materialia 116 (2016) 188–199.

[11] D. Raabe, H. Springer, I. Gutierrez-Urrutia, F. Roters, M. Bausch, J.-B. Seol, M. Koyama et al., Alloy Design, Combinatorial Synthesis, and Microstructure–Property Relations for Low-Density Fe-Mn-Al-C Austenitic Steels, JOM 66 (2014) 1845–1856.

[12]   I. Gutierrez-Urrutia, D. Raabe, High strength and ductile low density austenitic FeMnAlC steels, Materials Science and Technology 30 (2014) 1099–1104.

[13]   R.A. Howell, Army Research Lab, D.C. van Aken, A Literature Review of Age Hardening Fe-Mn-Al-C Alloys, Iron & Steel Technology Vol. 6 (2009) 193–212.

[14]   F. Brasche, C. Haase, M. Lipińska-Chwałek, J. Mayer, D.A. Molodov, Combined κ-carbide precipitation and recovery enables ultra-high strength and ductility in light-weight steels, Materials Science and Engineering: A 795 (2020) 139928.

[15]   F. Kies, X. Wu, B. Hallstedt, Z. Li, C. Haase, Enhanced precipitation strengthening of multi-principal element alloys by κ- and B2-phases, Materials & Design 198 (2021) 109315.

[16]   M. Abramova, A. Raab, R.Z. Valiev, A. Khannanova, C.S. Lee, J.N. Kim, G.H. Jang et al., Tailoring Extra-Strength of a TWIP Steel by Combination of Multi-Pass Equal-Channel Angular Pressing and Warm Rolling, Metals 11 (2021) 518.

[17]   L. Wang, J.A. Benito, J. Calvo, J.M. Cabrera, Equal channel angular pressing of a TWIP steel, J Mater Sci 52 (2017) 6291–6309.

[18]   A.S. Hamada, L.P. Karjalainen, High-cycle fatigue behavior of ultrafine-grained austenitic stainless and TWIP steels, Materials Science and Engineering: A 527 (2010) 5715–5722.

[19]   C.W. Shao, P. Zhang, Y.K. Zhu, Z.J. Zhang, J.C. Pang, Z.F. Zhang, Improvement of low-cycle fatigue resistance in TWIP steel by regulating the grain size and distribution, Acta Materialia 134 (2017) 128–142.

[20]   K.-G. Chin, H.-J. Lee, J.-H. Kwak, J.-Y. Kang, B.-J. Lee, Thermodynamic calculation on the stability of (Fe,Mn)3AlC carbide in high aluminum steels, Journal of Alloys and Compounds 505 (2010) 217–223.

[21]   P. Chen, X. Li, H. Yi, The κ-Carbides in Low-Density Fe-Mn-Al-C Steels, Metals 10 (2020) 1021.

[22]   J.B. Seol, A Brief Review of κ-Carbide in Fe-Mn-Al-C Model Alloys, AM 48 (2018) 117–121.

[23]   C. Haase, C. Zehnder, T. Ingendahl, A. Bikar, F. Tang, B. Hallstedt, W. Hu et al., On the deformation behavior of κ-carbide-free and κ-carbide-containing high-Mn light-weight steel, Acta Materialia 122 (2017) 332–343.

[24]   J.D. Yoo, K.-T. Park, Microband-induced plasticity in a high Mn–Al–C light steel, Materials Science and Engineering: A 496 (2008) 417–424.

[25]   J.D. Yoo, S.W. Hwang, K.-T. Park, Origin of Extended Tensile Ductility of a Fe-28Mn-10Al-1C Steel, Metall and Mat Trans A 40 (2009) 1520–1523.

[26]   S.-D. Kim, J.Y. Park, S.-J. Park, J.H. Jang, J. Moon, H.-Y. Ha, C.-H. Lee et al., Direct observation of dislocation plasticity in high-Mn lightweight steel by in-situ TEM, Scientific reports 9 (2019) 15171.

[27]   K.-T. Park, Tensile deformation of low-density Fe–Mn–Al–C austenitic steels at ambient temperature, Scripta Materialia 68 (2013) 375–379.

[28]   C. Coupeau, J.-C. Girard, J. Rabier, Scanning Probe Microscopy and Dislocations, in: Elsevier, 2004, pp. 273–338.

[29]   X.-f. Zhang, H. Yang, D.-p. Leng, L. Zhang, Z.-y. Huang, G. Chen, Tensile Deformation Behavior of Fe-Mn-Al-C Low Density Steels, J. Iron Steel Res. Int. 23 (2016) 963–972.

[30]   O.A. Zambrano, A general perspective of Fe–Mn–Al–C steels, J Mater Sci 53 (2018) 14003–14062.

[31]   K. Choi, C.-H. Seo, H. Lee, S.K. Kim, J.H. Kwak, K.G. Chin, K.-T. Park et al., Effect of aging on the microstructure and deformation behavior of austenite base lightweight Fe–28Mn–9Al–0.8C steel, Scripta Materialia 63 (2010) 1028–1031.

[32]   V. Gerold, H.P. Karnthaler, On the origin of planar slip in f.c.c. alloys, Acta Metallurgica 37 (1989) 2177–2183.

[33]   H.P. Karnthaler, B. Schügerl, Dislocation Structures in Plastically Deformed, Disordered Ni3Fe, in: Strength of Metals and Alloys, Elsevier, 1979, pp. 205–210.

[34]   K.-T. Park, K.G. Jin, S.H. Han, S.W. Hwang, K. Choi, C.S. Lee, Stacking fault energy and plastic deformation of fully austenitic high manganese steels, Materials Science and Engineering: A 527 (2010) 3651–3661.

[35]   M.T. Jahn, S.C. Chang, Y.H. Hsiao, Transverse tensile and fatigue properties of Fe-Mn-Al-C alloys, J Mater Sci Lett 8 (1989) 723–724.

[36]   I.S. Kalashnikov, O. Acselrad, T. Kalichak, M.S. Khadyyev, L.C. Pereira, Behavior of Fe-Mn-Al-C Steels during Cyclic Tests, Journal of Materials Engineering and Performance 9 (2000) 334–337.

[37]   N.J. Ho, L.T. Wu, S.C. Tjong, Cyclic deformation of duplex Fe-30Mn-10Al-0.4C alloy at room temperature, Materials Science and Engineering: A 102 (1988) 49–55.

[38]   N.J. Ho, S.C. Tjong, Cyclic stress-strain behaviour of austenitic Fe-29.7Mn-8.7A1-1.04C alloy at room temperature, Materials Science and Engineering 94 (1987) 195–202.

[39]   S.C. Chang, Y.H. Hsiau, M.T. Jahn, Tensile and fatigue properties of Fe-Mn-Al-C alloys, J Mater Sci 24 (1989) 1117–1120.

[40]   S.C. Tjong, N.J. Ho, Transmission electron microscopy observations of strain-induced martensitic formation in fatigued Fe□21Mn□2.5Al alloy, Materials Science and Engineering: A 102 (1988) 125–130.

[41]   S.C. Tjong, N.J. Ho, Transmission electron microscopy studies of the dislocation microstructures in fatigued Fe-8.7Al-29.7Mn-1.04C alloy, Materials Science and Engineering 91 (1987) 161–167.

[42]   S.C. Tjong, Low cycle fatigue behavior of an austenitic Fe□25Mn□8Al□1C alloy containing grain boundary precipitates, Materials Science and Engineering: A 203 (1995) L13-L16.

[43]   N.J. Ho, C.M. Chen, S.C. Tjong, Cyclic softening of age hardened Fe□Mn□Al□C alloys containing coherent precipitates, Scripta Metallurgica 21 (1987) 1319–1322.

[44]   N. Schell, A. King, F. Beckmann, T. Fischer, M. Müller, A. Schreyer, The High Energy Materials Science Beamline (HEMS) at PETRA III, MSF 772 (2013) 57–61.

[45]   C. Haase, L.A. Barrales-Mora, F. Roters, D.A. Molodov, G. Gottstein, Applying the texture analysis for optimizing thermomechanical treatment of high manganese twinning-induced plasticity steel, Acta Materialia 80 (2014) 327–340.

[46]   C. Haase, M. Kühbach, L.A. Barrales-Mora, S.L. Wong, F. Roters, D.A. Molodov, G. Gottstein, Recrystallization behavior of a high-manganese steel, Acta Materialia 100 (2015) 155–168.

[47]   V. Hauk, H. Behnken, Structural and residual stress analysis by nondestructive methods: Evaluation - application - assessment, Elsevier, Amsterdam, 2006.

[48]   I.S. Kalashnikov, O. Acselrad, A. Shalkevich, L.D. Chumakova, L.C. Pereira, Heat treatment and thermal stability of FeMnAlC alloys, Journal of Materials Processing Technology 136 (2003) 72–79.

[49]   W.K. Choo, J.H. Kim, J.C. Yoon, Microstructural change in austenitic Fe-30.0wt%Mn-7.8wt%Al-1.3wt%C initiated by spinodal decomposition and its influence on mechanical properties, Acta Materialia 45 (1997) 4877–4885.

[50]   M. Piston, L. Bartlett, K.R. Limmer, D.M. Field, Microstructural Influence on Mechanical Properties of a Lightweight Ultrahigh Strength Fe-18Mn-10Al-0.9C-5Ni (wt%) Steel, Metals 10 (2020) 1305.

[51]   W. Song, W. Zhang, J. von Appen, R. Dronskowski, W. Bleck, κ-Phase Formation in Fe-Mn-Al-C Austenitic Steels, steel research international 86 (2015) 1161–1169.

[52]   C. Mapelli, S. Barella, A. Gruttadauria, D. Mombelli, M. Bizzozero, X. Veys, γ Decomposition in Fe–Mn–Al–C lightweight steels, Journal of Materials Research and Technology 9 (2020) 4604–4616.

[53]   S. Picak, T. Wegener, S.V. Sajadifar, C. Sobrero, J. Richter, H. Kim, T. Niendorf et al., On the low-cycle fatigue response of CoCrNiFeMn high entropy alloy with ultra-fine grain structure, Acta Materialia 205 (2021) 116540.

[54]   T. Niendorf, C. Lotze, D. Canadinc, A. Frehn, H.J. Maier, The role of monotonic pre-deformation on the fatigue performance of a high-manganese austenitic TWIP steel, Materials Science and Engineering: A 499 (2009) 518–524.

[55]   H.-G. Lambers, C.J. Rüsing, T. Niendorf, D. Geissler, J. Freudenberger, H.J. Maier, On the low-cycle fatigue response of pre-strained austenitic Fe61Mn24Ni6.5Cr8.5 alloy showing TWIP effect, International Journal of Fatigue 40 (2012) 51–60.

[56]   T. Wegener, F. Brenne, A. Fischer, T. Möller, C. Hauck, S. Auernhammer, T. Niendorf, On the structural integrity of Fe-36Ni Invar alloy processed by selective laser melting, Additive Manufacturing 37 (2021) 101603.

[57]   T. Niendorf, T. Wegener, Z. Li, D. Raabe, Unexpected cyclic stress-strain response of dual-phase high-entropy alloys induced by partial reversibility of deformation, Scripta Materialia 143 (2018) 63–67.

[58]   H.P. Klug, L.E. Alexander, X-Ray diffraction procedures: For polycrystalline and amorphous materials, Wiley, New York, 1976.

[59]   C. Scott, B. Remy, J.-L. Collet, A. Cael, C. Bao, F. Danoix, B. Malard et al., Precipitation strengthening in high manganese austenitic TWIP steels, IJMR 102 (2011) 538–549.

[60]   D.T. Raske, J. Morrow, Mechanics of Materials in Low Cycle Fatigue Testing, in: R.M. Wetzel, L.F. Coffin (Eds.), Manual on Low Cycle Fatigue Testing, ASTM International, 100 Barr Harbor Drive, PO Box C700, West Conshohocken, PA 19428-2959, 1969, 1-1-26.

[61]   R.M. Wetzel, L.F. Coffin (Eds.), Manual on Low Cycle Fatigue Testing, ASTM International, 100 Barr Harbor Drive, PO Box C700, West Conshohocken, PA 19428-2959, 1969.

[62]   A. Nagesha, Influence of temperature on the low cycle fatigue behaviour of a modified 9Cr–1Mo ferritic steel, International Journal of Fatigue 24 (2002) 1285–1293.

[63]   H. Mughrabi, Microstructural mechanisms of cyclic deformation, fatigue crack initiation and early crack growth, Philosophical transactions. Series A, Mathematical, physical, and engineering sciences 373 (2015).

[64]   Q. Xin, Durability and reliability in diesel engine system design, Diesel Engine System
        Design (2013) 113–202.